

Supporting Information

Enhanced Breakthrough Efficiency by a Chemically Stable Porous Coordination Polymer with Optimized Nanochannel

Haifei Cao^{†#}, Zhiyong Lu^{‡#}, Kim Hyeon-Deuk[§], I-Ya Chang[§], Yang Wang[†], Zhifeng Xin^{//}, Jingui Duan^{†*}, and Wanqin Jin[†]

[†]State Key Laboratory of Materials-Oriented Chemical Engineering, College of Chemical Engineering, Nanjing Tech University, Nanjing 210009, China.

[‡]College of Mechanics and Materials, Hohai University, Nanjing, 210098, China

[§]Department of Chemistry, Kyoto University, Yoshida, Sakyo-ku, Kyoto, 606-8502, Japan

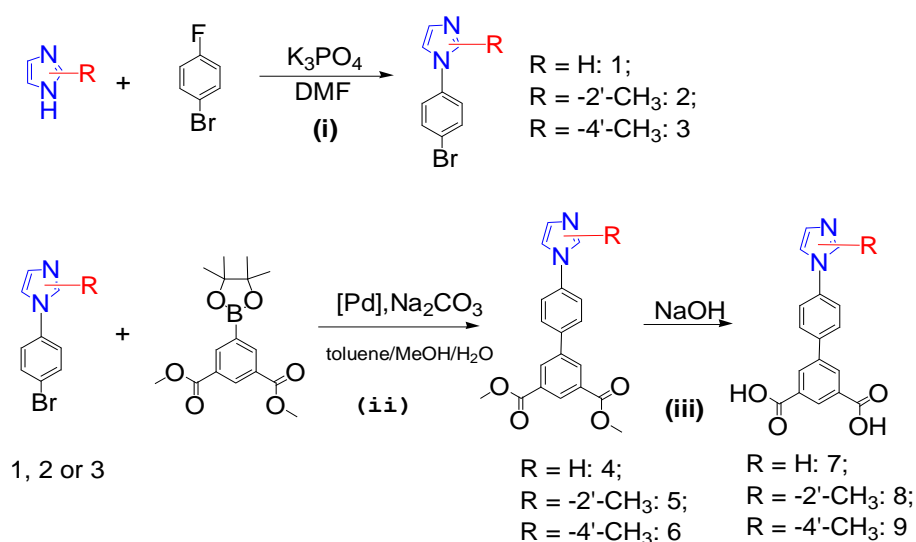
^{//}Institute of Molecule Engineering & Applied Chemistry, Anhui University of Technology, Maanshan 243002, China

*Email: duanjingui@njtech.edu.cn

Materials and methods

All air-sensitive reactions were carried out under a dry nitrogen atmosphere using standard Schleck techniques. The elemental analysis was carried out with a Perkin-Elmer 240C elemental analyzer. The Fourier-transform Infrared (FT-IR) spectra were recorded from KBr pellets in the range of 4000–500 cm^{-1} on a VECTOR 22 spectrometer. Thermogravimetric analyses (TGA) were performed using a STA 209 F1 (NETZSCH Instruments) thermo-microbalance, heating from room temperature to 650°C at a rate of 10°C min^{-1} under nitrogen flow. Simulated powder patterns from single-crystal X-ray diffraction data were generated using Mercury 1.4.2 software. *In situ* absorption spectra were measured with a PerkinElmer Lambda 950 UV–vis spectrophotometer. ^1H NMR and ^{13}C NMR spectra were recorded on a Bruker Advance III 600 MHz NMR Spectrometer. The powder X-ray diffraction patterns (PXRD) measurements were carried on a Bruker axS D8 Advance 40kV, 40mA for $\text{CuK}\alpha$ ($\theta = 1.5418 \text{ \AA}$) with a scan rate of 0.2 s/deg at room temperature.

Ligand synthesis



Scheme S1. Synthesis of series of ligands of 7 (4'-(1H-imidazol-1-yl)-[1,1'-biphenyl]-3,5-dicarboxylic acid: H_2NL^1), 8 (4'-(2-methyl-1H-imidazol-1-yl)-[1,1'-biphenyl]-3,5-dicarboxylic acid: H_2NL^2) and 9 (4'-(4-methyl-1H-imidazol-1-yl)-[1,1'-biphenyl]-3,5-dicarboxylic acid: H_2NL^3).

Synthesis of 1, 2 and 3

Same experiment condition, except corresponded imidazole derivatives, were used for ligands syntheses. Here, only the synthesis of H_2NL^1 was detailed.

1H-imidazole (1.4 g, 20.5 mmol), 1-bromo-4-fluorobenzene (7.1 g, 40.6 mmol), K_3PO_4 (21.2 g, 100.0 mmol) were added in DMF (200 mL). The reaction system was subsequently heated at reflux for 16 hours. After the temperature cooling down, the reaction mixture was filtered. The filtrate was extracted by adding water (400 mL) and EtOAc (200 × 3 mL), and then concentrated. The residue was purified by silica gel column chromatography using EtOAc/Hexane to give 1 as white solid in about 45.9% yield (2.1 g, 9.4 mmol). ^1H NMR (CDCl_3) of 1: 7.22

(s, 1H), 7.25(s, 1H), 7.27 (d, 2H), 7.60 (d, 2H), 7.83(s, 1H). IR (KBr, cm^{-1}) of 1: 3108, 1891, 1591, 1505, 1409, 1302, 1261, 1239, 1104, 1057, 1011, 956, 908, 826, 784, 764, 660. ^1H NMR (CDCl_3) of 2: 2.34 (s, 3H), 6.96 (d, 1H), 7.02 (d, 1H), 7.16 (d, 2H), 7.60 (d, 2H). IR (KBr, cm^{-1}) of 2: 3091, 1590, 1501, 1416, 1307, 1178, 1139, 1101, 1072, 980, 835, 808, 769, 732, 707, 669, 639. ^1H NMR (CDCl_3) of 3: 2.27 (s, 6H), 6.95 (s, 1H), 7.15 (d, 1H), 7.22 (d, 2H), 7.56 (d, 2H). IR (KBr, cm^{-1}): 3097, 1594, 1443, 1292, 1243, 1108, 1066, 1005, 967, 916, 826, 748, 659, 614.

Synthesis of 4, 5 and 6

Compound 1 (2.0 g, 8.9 mmol), 5-(4,4,5,5-Tetramethyl-[1,3,2]dioxaborolan-2-yl)- isophthalic acid dimethyl ester (3.7 g, 11.6 mmol), Na_2CO_3 (1.7 g, 16.1 mmol), $\text{Pd}(\text{PPh}_3)_4$ (0.4 g, 0.36 mmol) were added in mixed solvents of deionized water (20 mL), MeOH (20 mL), toluene (65 mL). The reaction system was bubbled by N_2 for 30 mins and subsequent heating at reflux for 24 hours. After the temperature cooling down, the reaction mixture was concentrated by the removal of toluene and MeOH by evaporation. The residue was extracted by adding water (80 mL) and CH_2Cl_2 (100 \times 3 mL), and then concentrated. The organic phase was concentrated by rotary evaporation. The residue was purified by silica gel column chromatography using EtOAc/Hexane (with drop of MeOH) to give the compound 4 as white solid with yield of 73.1% (3.3 g, 9.8 mmol). ^1H NMR (CDCl_3) of 4: 4.00 (s, 6H), 7.35 (s, 1H), 7.52 (d, 2H), 7.78 (d, 2H), 7.93 (s, 1H), 8.45(d, 2H), 8.70 (t, 1H). IR (KBr, cm^{-1}): 3148, 3128, 2958, 1707, 1612, 1528, 1494, 1454, 1431, 1349, 1317, 1278, 1255, 1231, 1138, 1074, 991, 828, 752, 658. ^1H NMR (CDCl_3) of 5: 2.42 (s, 3H), 4.00(s, 6H), 7.06(d, 2H), 7.41(d, 2H), 7.77(d, 2H), 8.49(d, 2H), 8.70 (t, 1H). IR (KBr, cm^{-1}): 3603, 3421, 3108, 2949, 1731, 1518, 1436, 1415, 1249, 995, 845, 757. ^1H NMR (CDCl_3) of 6: 2.34(s, 3H), 4.00(s, 6H), 7.07(s, 1H), 7.47(d, 2H), 7.75(d, 2H), 7.82(d, 2H), 8.47(d, 2H), 8.68 (t, 1H). IR (KBr, cm^{-1}): 3118, 2953, 1718, 1608, 1526, 1490, 1432, 1343, 1287, 1243, 1139, 1075, 997, 970, 832, 754, 716, 619, 566.

Synthesis of Compound 7 (H_2NL^1), 8 (H_2NL^2) and 9 (H_2NL^3)

Compound 4 (1.7 g, 4.7 mmol), sodium hydroxide (2.0 g, 50.0 mmol) was added to solution of THF (30 mL)/MeOH (30 mL)/ H_2O (60 mL). The reaction system was stirred at 80°C for 10 hours. After the temperature cooling down, the organic solvents were evaporated and HCl (conc.) was added dropwise with strong stirring, precipitating the product. The flask was cooled to 0°C to ensure complete precipitation, the solids collected by filtration, washed thoroughly with water and dried at 80°C to give the desired product of 7 (H_2NL^1) (1.4 g, 4.6 mmol) with yield of 99.0%. ^1H NMR ($\text{DMSO}-d_6$) of 7 (H_2NL^1): 7.88 (s, 1H), 7.94 (s, 4H), 8.32(t, 1H), 8.35(d, 2H), 8.41(t, 1H), 9.82 (s, 1H). IR (KBr, cm^{-1}) of 7 (H_2NL^1): 1705, 1596, 1538, 1452, 1237, 834, 755, 668, 626. ^1H NMR ($\text{DMSO}-d_6$) of 8 (H_2NL^2): 2.62 (s, 3H), 7.78(s, 1H), 7.81 (d, 2H), 7.95 (d, 2H), 8.03 (d, 2H), 8.45 (d, 2H), 8.51(t, 1H). IR (KBr, cm^{-1}) of 8 (H_2NL^2): 1727, 1694, 1530, 1412, 1249, 1215, 926, 862, 768, 731, 668. ^1H NMR ($\text{DMSO}-d_6$) of 9 (H_2NL^3): 2.14 (s, 3H), 7.51 (s, 1H), 7.69 (d, 2H), 7.82 (d, 2H), 8.28 (s, 1H), 8.35 (d, 2H), 8.41 (t, 1H). IR (KBr, cm^{-1}) of 9 (H_2NL^3): 1694, 1632, 1543, 1453, 1419, 1363, 1290, 1204, 1076, 917, 840, 771, 682, 614.

Table S1. Crystal Data for NTU-23, NTU-24 and NTU-25.

	NTU-23	NTU-24	NTU-25
Empirical formula	C ₁₇ H ₁₀ CuN ₂ O ₄	C ₁₈ H ₁₂ CuN ₂ O ₄	C ₁₈ H ₁₂ CuN ₂ O ₄
Formula weight	369.82	383.85	383.85
Crystal system	trigonal	trigonal	trigonal
Space group	<i>R</i> -3 <i>c</i>	<i>R</i> -3 <i>c</i>	<i>R</i> -3 <i>c</i>
Unit cell dimensions	<i>a</i> = 18.534(5) Å <i>c</i> = 83.78(3) Å	<i>a</i> = 18.866(5) Å <i>c</i> = 83.32(4) Å	<i>a</i> = 18.231(5) Å <i>c</i> = 84.42(5) Å
Volume	24924(19) Å ³	25683(21) Å ³	24300(23) Å ³
Z	36	36	36
Density (calculated)	0.887 g/cm ³	0.893 g/cm ³	0.944 g/cm ³
Mu (MoKa)	0.802 mm ⁻¹	0.780 mm ⁻¹	0.824 mm ⁻¹
<i>F</i> ₍₀₀₀₎	6732	7020	7020
Theta min-max	1.4, 25.0	1.3, 25.0	1.4, 24.0
Index ranges	-22 ≤ <i>h</i> ≤ 22 -19 ≤ <i>k</i> ≤ 22 -99 ≤ <i>l</i> ≤ 99	-19 ≤ <i>h</i> ≤ 22 -22 ≤ <i>k</i> ≤ 22 -98 ≤ <i>l</i> ≤ 98	-19 ≤ <i>h</i> ≤ 20 -20 ≤ <i>k</i> ≤ 20 -96 ≤ <i>l</i> ≤ 94
Tot, Uniq Data, R(int)	56008, 4917, 0.174	58085, 5065, 0.058	48947, 4281, 0.144
Observed data [<i>I</i> > 2σ(<i>I</i>)]	2840	3998	2763
<i>N</i> _{ref} , <i>N</i> _{par}	4917, 205	5065, 215	4281, 206
<i>R</i> ₁ , <i>wR</i> ₂ , <i>S</i>	0.0991, 0.3189, 1.02	0.0790, 0.2790, 1.10	0.1250, 0.3963, 1.39
Max Shift	0	0	0

$$R = \frac{\sum ||F_o| - |F_c||}{\sum |F_o|}, \quad wR = \left\{ \frac{\sum [w (|F_o|^2 - |F_c|^2)^2]}{\sum [w (|F_o|^4)]} \right\}^{1/2} \quad \text{and} \quad w = \frac{1}{[\sigma^2(F_o^2) + (0.1452P)^2]} \quad \text{where} \quad P = \frac{(F_o^2 + 2F_c^2)}{3}$$

Structural details

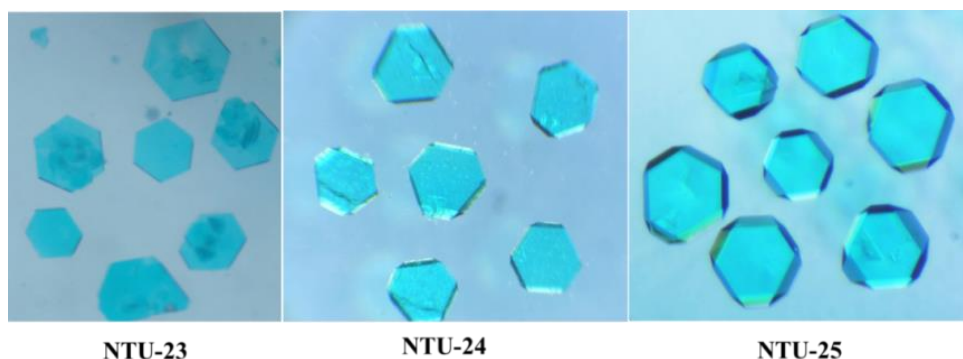


Figure S1. The photograph of three polyhedral crystals.

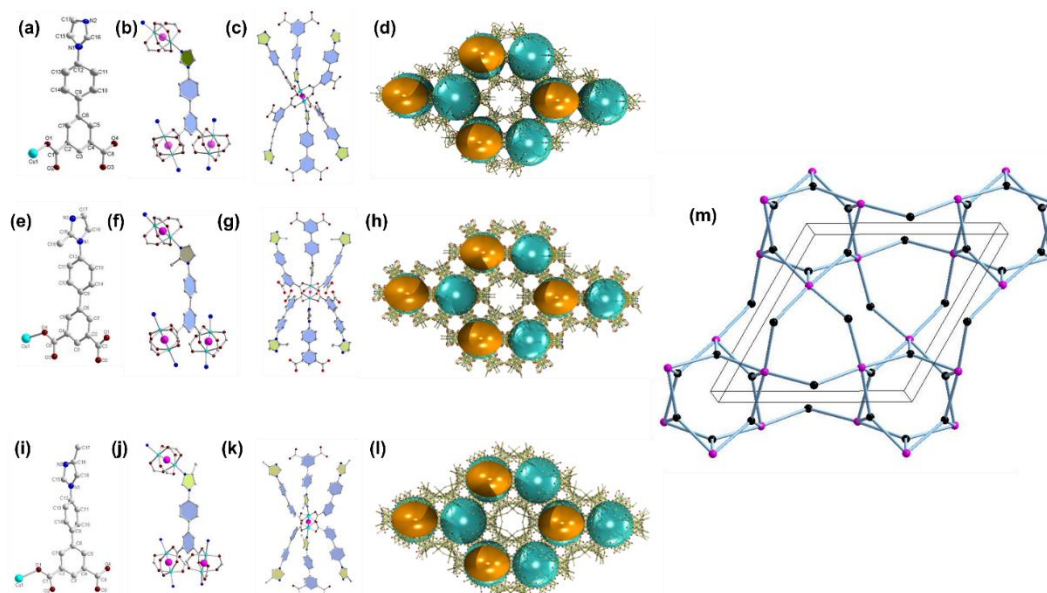


Figure S2. Structure views of NTU-23 to -25: Asymmetric unit of NTU-23 (a); Ligand connection of NTU-23. One ligand was bridged by three Cu clusters (b); View of cluster connection of NTU-23. One cluster was coordinated by six ligands (c); View of packed framework of cage A (turquoise) and cage B (yellow) of NTU-23 along *c*-axis (d); Asymmetric unit of NTU-24 (e); Ligand connection of NTU-24. One ligand was bridged by three Cu clusters (f); View of cluster connection of NTU-24. One cluster was coordinated by six ligands (g); View of packed framework of cage A (turquoise) and cage B (yellow) of NTU-24 along *c*-axis (h); Asymmetric unit of NTU-25 (i); Ligand connection of NTU-25. One ligand was bridged by three Cu clusters (j); View of cluster connection of NTU-25. One cluster was coordinated by six ligands (k); View of packed framework of cage A (turquoise) and cage B (yellow) of NTU-25 along *c*-axis (l); (3, 6)-connected **eea** net of NTU-23 to -25 (m).

Basic characterization

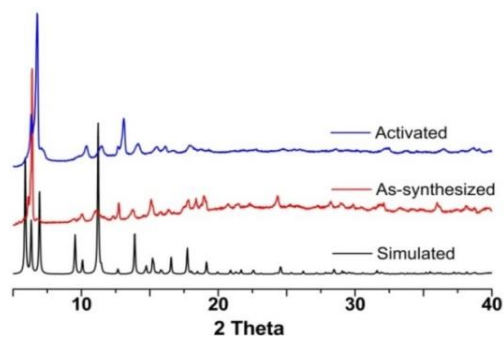


Figure S3. PXRD of simulated, as-synthesized and activated NTU-23.

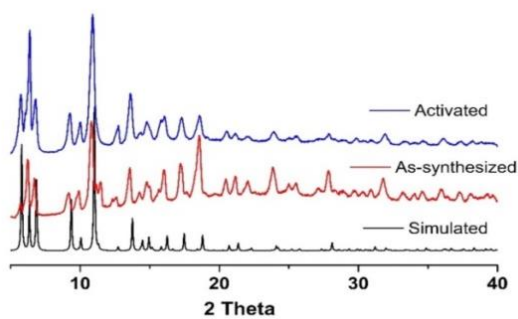


Figure S4. PXRD of simulated, as-synthesized and activated NTU-24.

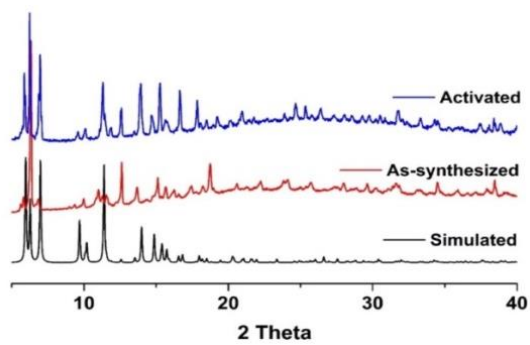


Figure S5. PXRD of simulated, as-synthesized and activated NTU-25.

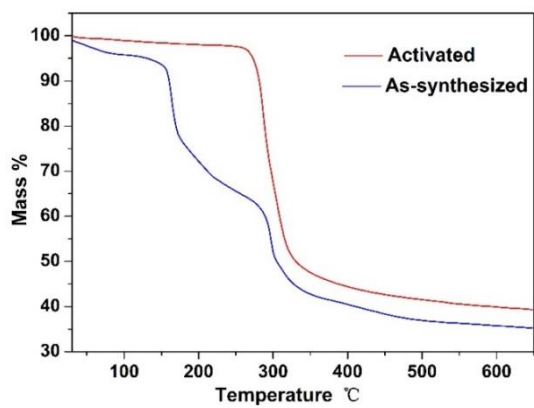


Figure S6. TG of as-synthesized and activated NTU-23.

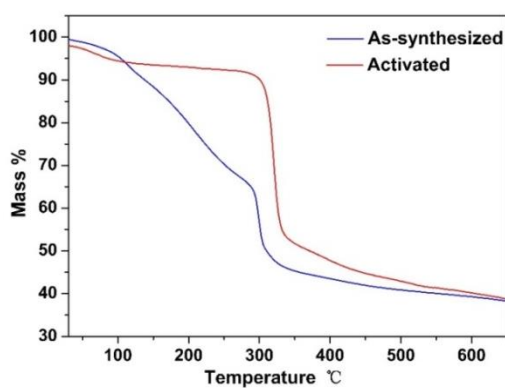


Figure S7. TG of as-synthesized and activated NTU-24.

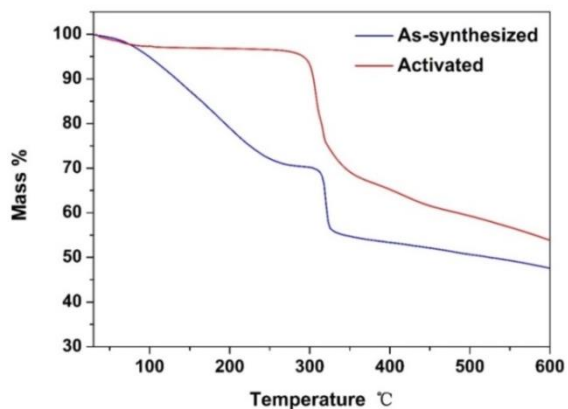


Figure S8. TG of as-synthesized and activated NTU-25.

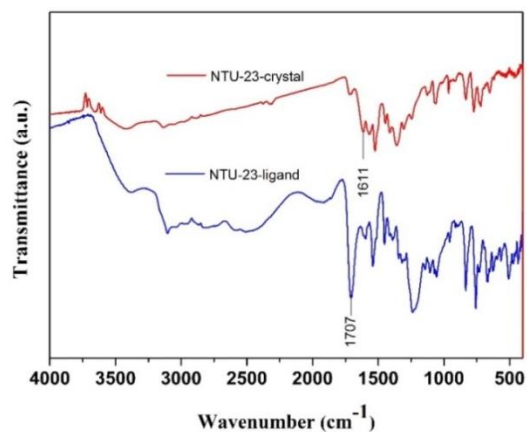


Figure S9. IR of H_2NL^1 and as-synthesized NTU-23.

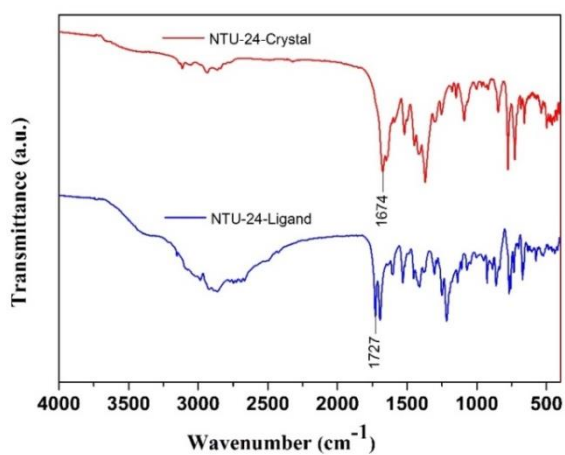


Figure S10. IR of H_2NL^2 and as-synthesized NTU-24.

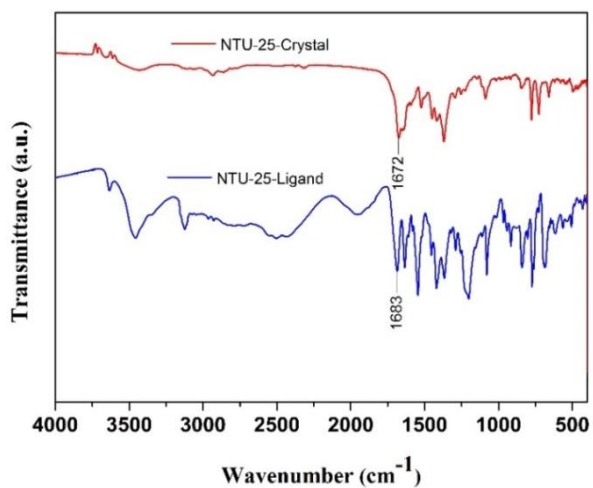


Figure S11. IR of H_3NL^3 and as-synthesized NTU-25.

Chemical stability test

For chemical treatment, fresh samples (about 100 mg for each) were soaked into three bottles (10 mL). HCl and NaOH were used to turn the pH of the solution to 2 and 12.

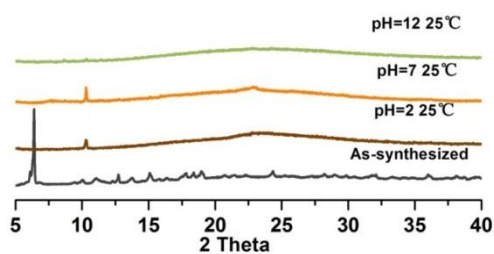


Figure S12. PXRD of chemically treated NTU-23.

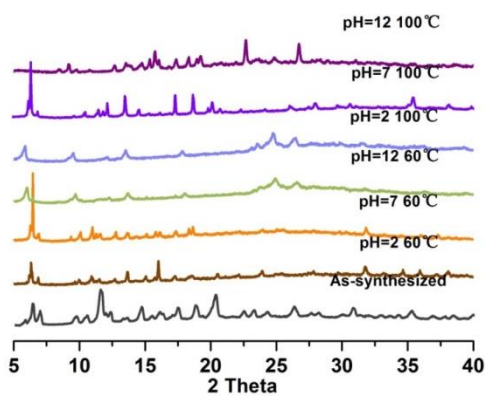


Figure S13. PXRD of chemically treated NTU-24.

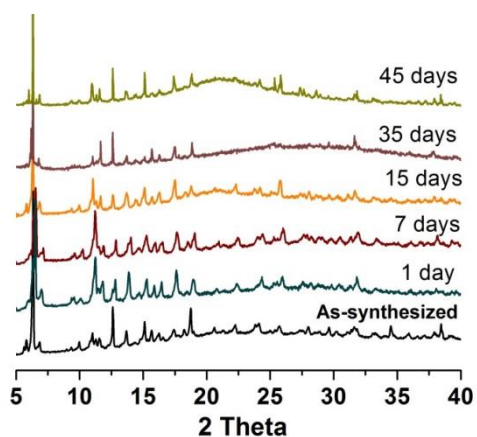


Figure S14. PXRD of water treated NTU-25: NTU-25 can keep the framework in water for 45 days at room temperature.

Sample activation

The solvent-exchanged sample was prepared by immersing the as-synthesized samples in DMF (1 day) and then dry EtOH (3 days) to remove the solvents. The sample was decanted every 8 hours and fresh solvents were replaced. The completely activated sample was obtained by heating the EtOH-exchanged sample at 120 °C under a dynamic high vacuum for 24 hours.

Adsorption experiments

In the gas adsorption measurement, ultra-high-purity grade of N₂, CH₄, C₂H₄, C₂H₆ and CO₂ gases were used throughout the adsorption experiments. All of the measured sorption isotherms have been repeated two times to confirm the reproducibility within experimental error. Gas adsorption isotherms were obtained using a Belsorp-mini volumetric adsorption instrument from BEL Japan Inc, using the volumetric technique. To provide high accuracy and precision in determining P / P_0 , the saturation pressure P_0 was measured throughout the N₂ analyses by means of a dedicated saturation pressure transducer, which allowed us to monitor the vapor pressure for each data point. A part of the N₂ sorption isotherm in the P / P_0 range 0.02–0.25 was fitted to the BET equation to estimate the BET surface area. Langmuir surface area calculation was performed using all data points. The pore size distribution was obtained from the GCMC method in the BEL Japan software package based on the N₂ adsorption at 77K. BET surface area (Langmuir area): 1850 (2000) m²/g for NTU-23; 1620 (1760) m²/g for NTU-24; 1540 (1690) m²/g for NTU-25. Calculated pore volume: 0.716 cm³/g for NTU-23; 0.628 cm³/g for NTU-24; 0.5927 cm³/g for NTU-25.

Binary mixture adsorption

IAST was used to predict binary mixture adsorption from the experimental pure-gas isotherms. In order to perform the integrations required by IAST, the single-component isotherms should be fitted by a proper model. There is no restriction on the choice of the model to fit the adsorption isotherm, but data over the pressure range under study should be fitted very precisely^[6]. Several isotherm models were tested to fit the experimental pure isotherms for CH₄, C₂H₄, C₂H₆ and CO₂ in NTU-24 and NTU-25, and the dual-site Langmuir-Freundlich equation was found to best fit the experimental data:

$$q = q_{m1} \cdot \frac{b_1 \cdot P^{1/n_1}}{1 + b_1 \cdot P^{1/n_1}} + q_{m2} \cdot \frac{b_2 \cdot P^{1/n_2}}{1 + b_2 \cdot P^{1/n_2}} \quad (1)$$

Here, P is the pressure of the bulk gas at equilibrium with the adsorbed phase (kPa), q is the adsorbed amount per mass of adsorbent (mol/kg), q_{m1} and q_{m2} are the saturation capacities of sites 1 and 2 (mol/kg), b_1 and b_2 are the affinity coefficients of sites 1 and 2 (1/kPa), and n_1 and n_2 represent the deviations from an ideal homogeneous surface. Figure 4c shows that the dual-site Langmuir-Freundlich equation fits the single-component isotherms extremely well. The R_2 values for all the fitted isotherms were over 0.99997. Hence, the fitted isotherm parameters were applied to perform the necessary integrations in IAST.

Estimation of the adsorption heats

A virial-type expression comprising the temperature-independent parameters a_i and b_i was employed to calculate the enthalpies of adsorption for CH₄, C₂H₄, C₂H₆ and CO₂ (at 273, 283 and 298 K) on NTU-24 and NTU-25. In each case, the data were fitted using the equation:

$$\ln P = \ln N + 1/T \sum_{i=0}^m a_i N^i + \sum_{i=0}^n b_i N^i \quad (2)$$

Here, P is the pressure expressed in Torr, N is the amount adsorbed in mmol/g, T is the temperature in K, a_i and b_i are virial coefficients, and m , n represents the number of coefficients required to adequately describe the isotherms (m and n were gradually increased until the contribution of extra added a and b coefficients was deemed to be statistically insignificant towards the overall fit, and the average value of the squared deviations from the experimental values was minimized):

$$Q_{st} = -R \sum_{i=0}^m a_i N^i \quad (3)$$

Here, Q_{st} is the coverage-dependent isosteric heat of adsorption and R is the universal gas constant.

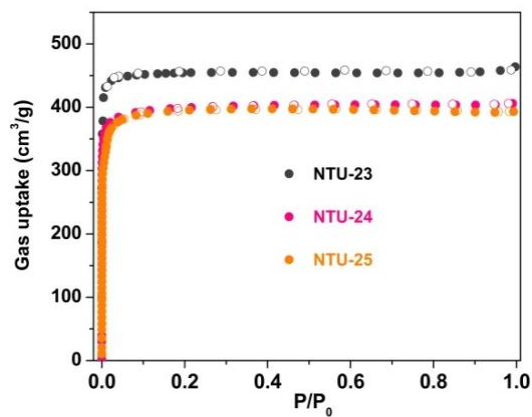


Figure S15. N₂ adsorption isotherms of NTU-23, -24, and -25 at 77 K.

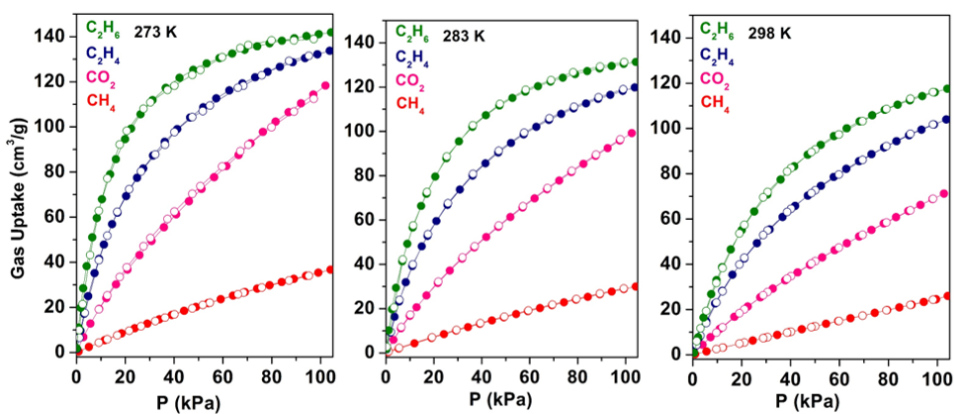


Figure S16. Single gas adsorption isotherms of NTU-24 at 273, 283K and 298K.

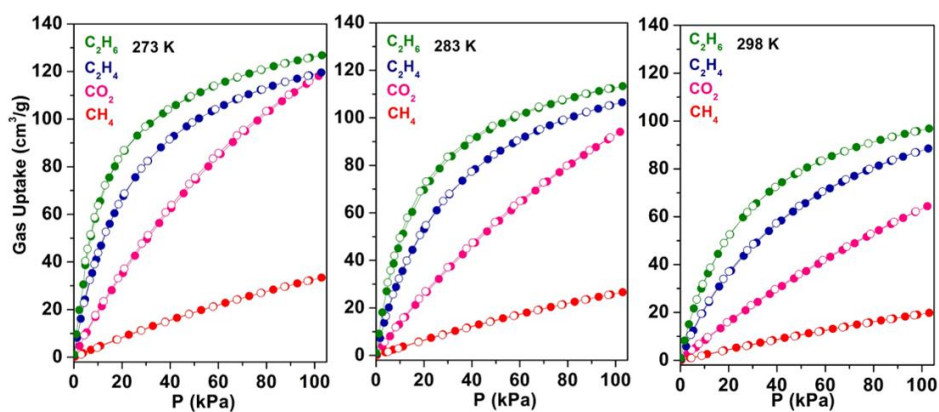


Figure S17. Single gas adsorption isotherms of NTU-25 at 273, 283K and 298K.

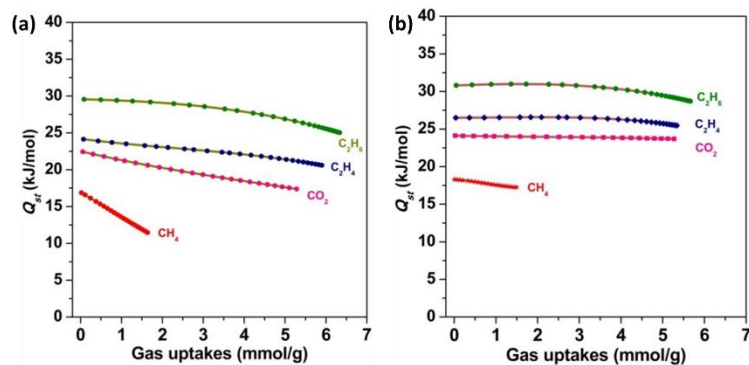


Figure S18. Calculated adsorption heats of NTU-24 (a) and NTU-25 (b).

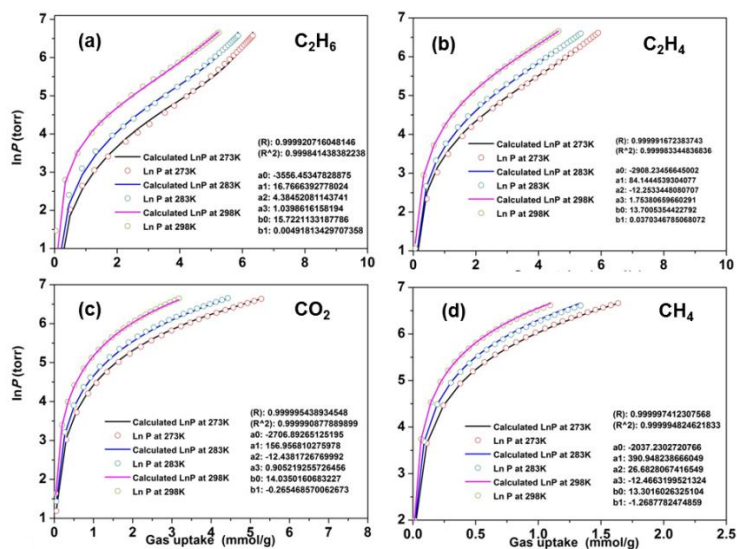


Figure S19. The calculated virial equation isotherms parameters fit to the experimental C_2H_6 (a), C_2H_4 (b), CO_2 (c) and CH_4 (d) data (at 273, 283 and 298K) of NTU-24.

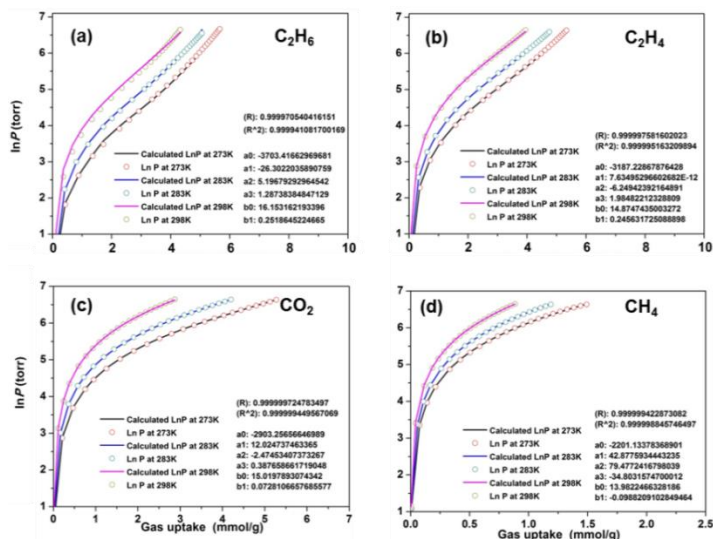


Figure S20. The calculated virial equation isotherms parameters fit to the experimental C_2H_6 (a), C_2H_4 (b), CO_2 (c) and CH_4 (d) data (at 273, 283 and 298K) of NTU-25.

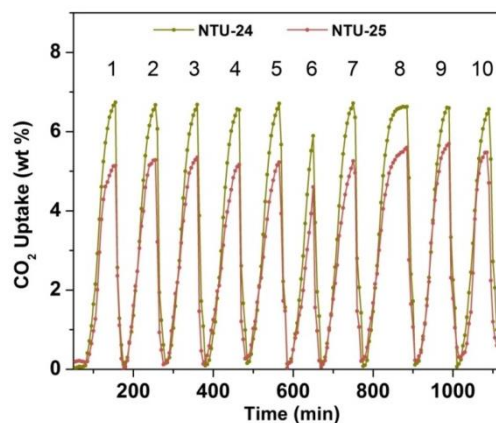


Figure S21. Dynamic CO₂ adsorption of NTU-24 and NTU-25 (flow rates are 50 mL·min⁻¹). The sample mass was normalized to 0% and max% at 120°C and 20°C, respectively. Importantly, after five adsorption cycles, we reduced equilibrium time from 10 to 1 min, and extended from 10 to 30 min, in the sixth and eighth cycle. The gas uptake decreased very a little in the sixth cycle and kept same in eighth. Once equilibrium program was reversed, such as cycle 7 and 9, CO₂ uptake fully recovered.

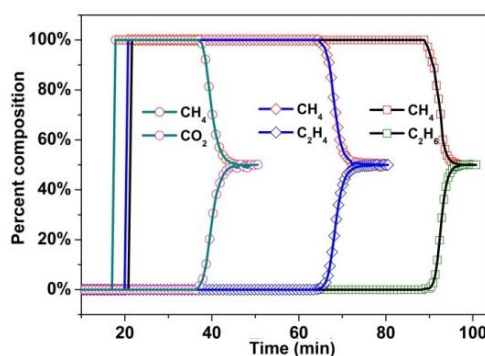


Figure S22. Breakthrough curves for a mixture of CH₄/CO₂, CH₄/C₂H₄ and CH₄/C₂H₆ (50:50 v/v) on NTU-24 at 273 K.

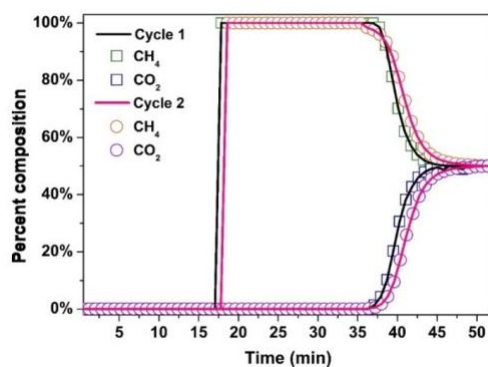


Figure S23. Recyclability of breakthrough tests of CH₄/CO₂ on NTU-24 at 273K.

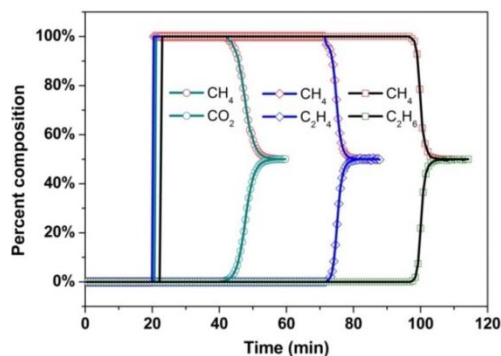


Figure S24. Breakthrough curves for a mixture of CH₄/CO₂, CH₄/C₂H₄ and CH₄/C₂H₆ (50:50 v/v) on NTU-25 at 273 K.

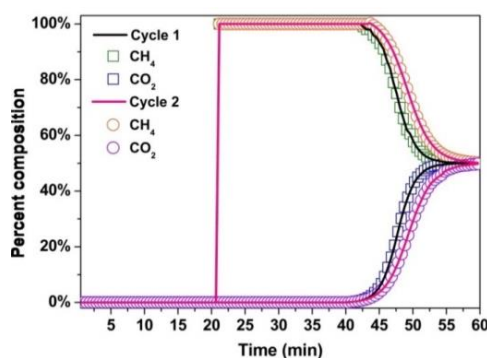


Figure S25. Recyclability of breakthrough tests of CH₄/CO₂ on NTU-25 at 273K.

Computational Methods

Structures (1) NTUs: The structures of Cage A and Cage B as well as their crucial local structures for the gas separation were cut from the bulk crystal structures of NTU-24 and NTU-25. The cut aromatic side-chains and carboxyl groups were replaced by H atoms. The XYZ coordinates of all the H atoms were optimized with the HF/3-21G(d) level in a gas phase while the other heavy-atom coordinates were fixed. (2) Small gas molecules: The structures of the small gas molecules, CH₄, C₂H₆, C₂H₄ and CO₂, were fully optimized without any constraint by the method of B3LYP/6-311G(d).

Cross sections The cross sections of the NTU materials and small gas molecules were estimated by their charge density surface with the isovalue of 0.002. As shown in Figure S26, the charge density surface with the isovalue of 0.002 almost coincides with the molecular surface formed by atomic spheres with the van der Waals Radii of composing atoms. Therefore, the current isovalue is reasonable to estimate the effective cross sections. The three-dimensional (3D) charge density surface was obtained by the following steps: (1) Wave functions of the optimized structures were calculated by the B3LYP/6-311G(d) method for all the atoms; (2) The total charge density was calculated from the converged wave function using the utility cubegen program of Gaussian 09 package; (3) The 3D charge density surface was visualized by the GaussView 5.0 package with the isovalue of 0.002.

Atomic charge The atomic charge was analyzed by the Natural Population Analysis (NPA)¹ implemented in the Gaussian 09 package. In all the atomic charge calculations, B3LYP/6-311G(d) was adopted.

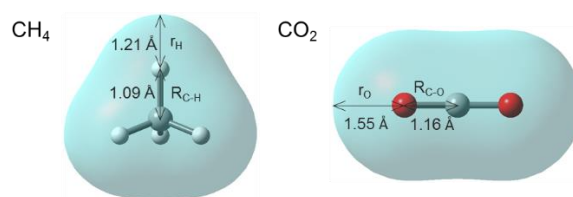


Figure S26. The charge density surface of CH₄ and CO₂ with the isovalue of 0.002. The effective atomic radii of hydrogen (H) and oxygen (O) were estimated as 1.21 and 1.55 Å, respectively, which are comparable to the conventional van der Waals Radii of H (1.1 ~ 1.2 Å) and O (1.3 ~ 1.6 Å)². Therefore, the density surface with the isovalue of 0.002 almost agrees with the molecular surface formed by atomic spheres of the van der Waals Radii, and it is reasonable to estimate the cross-section area of the NTU materials and the size of gas molecules with the current charge density surface.

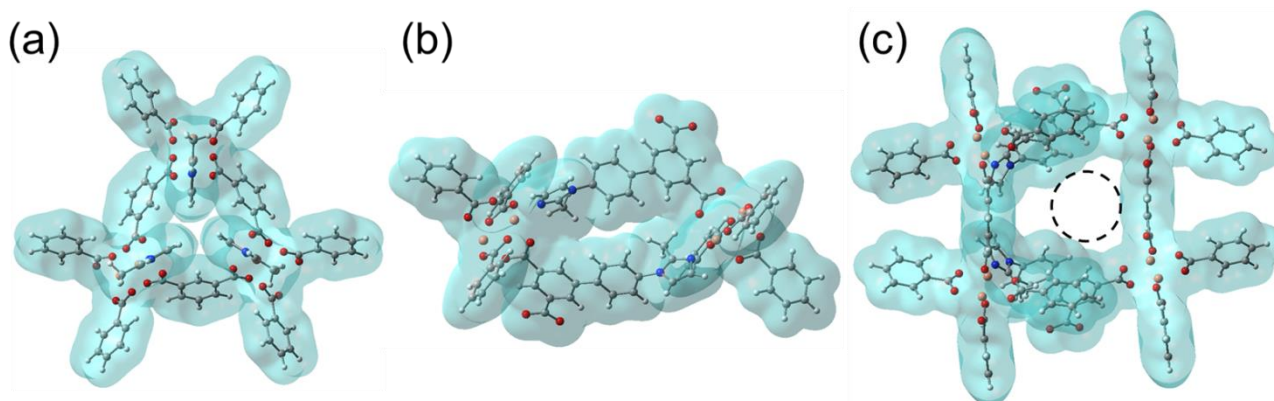


Figure S27. Effective size of channels along 001 plane (a), b-axis (b), and 0964 plane (c) of NTU-24 as well as the four molecules, estimated with the charge density which corresponds to the van der Waals radii. The channel along 001 plane where the three -CH₃ stretch against the bottle neck showed a little hole, which is different from the case of NTU-25. The longest length of the nanochannel along b-axis is even shorter, ~0.86 Å, in the NTU-24 case. In contrast, the channel along 0964 plane has enough space (~4.60 Å in diameter) for the four molecules to go through. Note that C₂H₆/C₂H₄/CO₂ have to align their molecular axes along the channel along 0964 plane to pass while CH₄ freely goes through it with any orientation, which achieved the present efficient gas separation of CH₄ from the other three molecules.

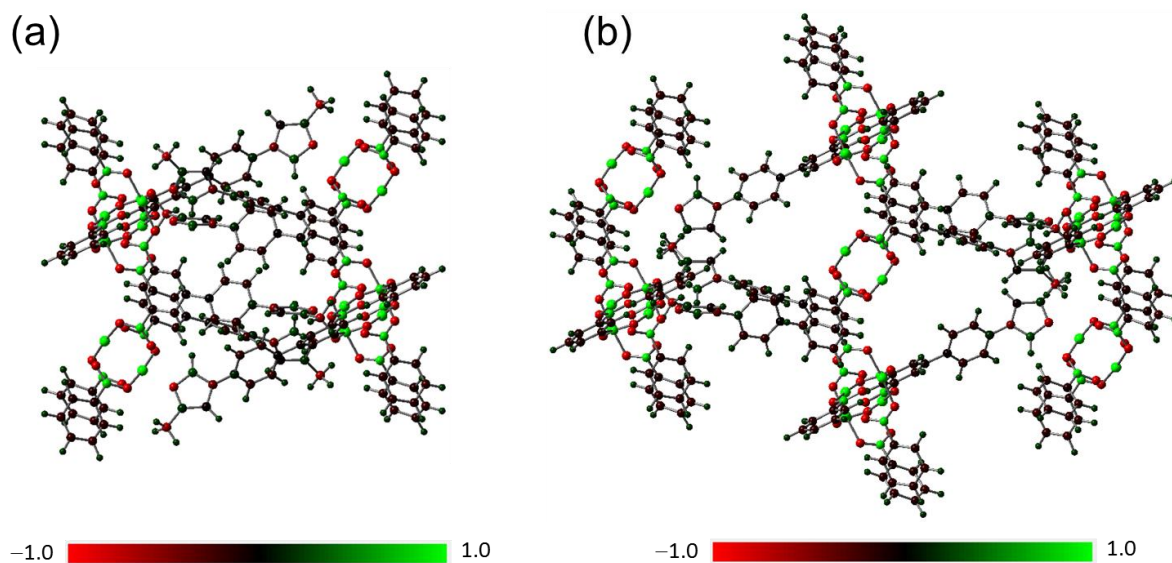


Figure S28. (a) Atomic charges calculated by the NPA of Cage A in NTU-25. (See Computational Methods in this SI) Since H atoms of the C_2H_6 molecule have positive charge, as shown in Figure S29, negatively charged O atoms outside Cage A can adsorb C_2H_6 through the weak hydrogen bonding. N atoms outside Cage A are also negatively charged while positively charged H atoms near the N atoms hinder the approaching of C_2H_6 , resulting in no adsorption to the N atoms. C_2H_6 placed inside Cage A was repelled from O atoms and moved toward the centre of Cage A because of the steric hindrance and repulsive force from positively charged C atoms located beside the O atoms of carboxyl ligands. We note that, since Cu atoms are fully coordinated by carboxyl groups and imidazole side chains, molecules cannot access the Cu atoms. (b) Atomic charges calculated by the NPA of Cage B in NTU-25. Negatively charged O atoms outside Cage B can adsorb C_2H_6 through the weak hydrogen bonding. However, because of the same reasons explained in (a), C_2H_6 placed inside Cage B was repelled from O atoms and moved toward the centre of Cage B. In conclusion, there are only two weak adsorption sites for the C_2H_6 molecule, that is, O atoms outside Cage A and Cage B in NTU-25. We also emphasize that the original adsorption forces of Cage A and Cage B are weak since all the atomic charges other than the Cu charge of approximately 1.30 are totally small; even O atoms have the atomic charge of approximately -0.74. The same conclusion holds also for NTU-23 and NTU-24 because the basic frameworks and composing atoms of the NTU crystals are similar other than inserting and shifting $-CH_3$, respectively.

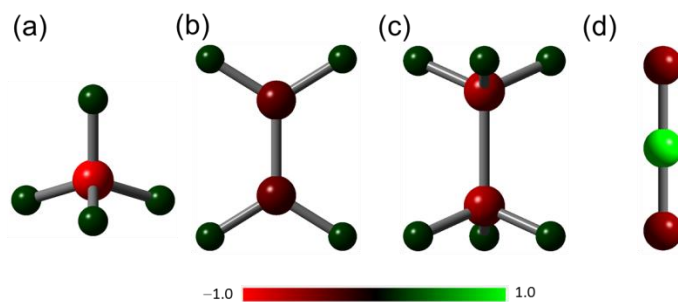


Figure S29. Atomic charges calculated by the NPA of CH_4 (a), C_2H_4 (b), C_2H_6 (c), and CO_2 (d).

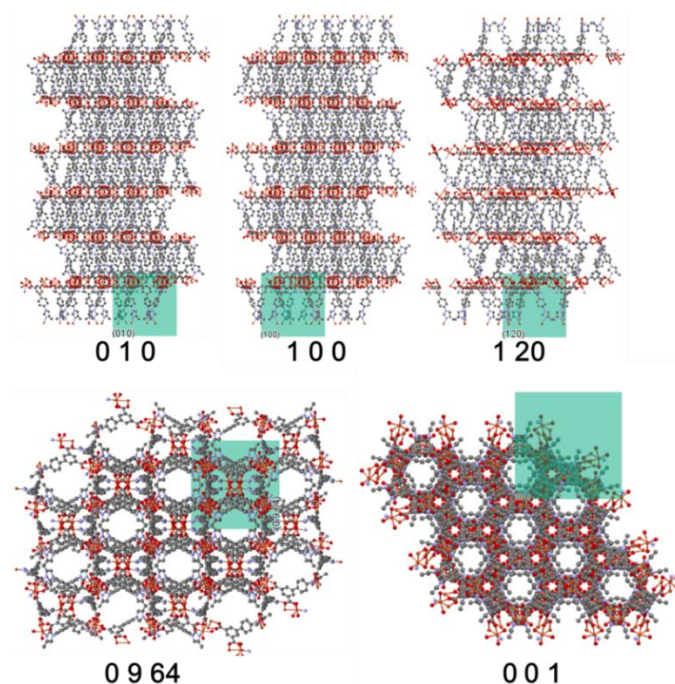


Figure S30. View of NTU-25 along different planes. The available channels can be found along planes of 0 0 1 and 0 9 64.

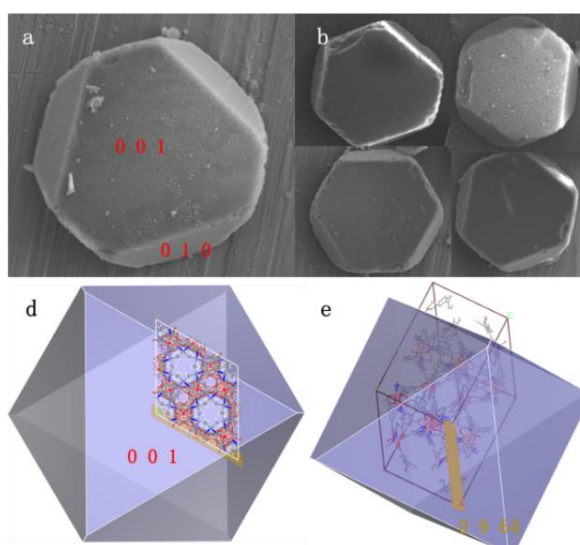


Figure S31. Crystal view of NTU-25 and its good morphology uniformity (a-b); Tridimensional BFDH morphology of NTU-25 drew out by Mercury software (c-d). From the combined view, the most exposed pores are the one along 0 0 1 plane in all crystals. The pore along 0 9 64 plane was fully covered by crystal packing.

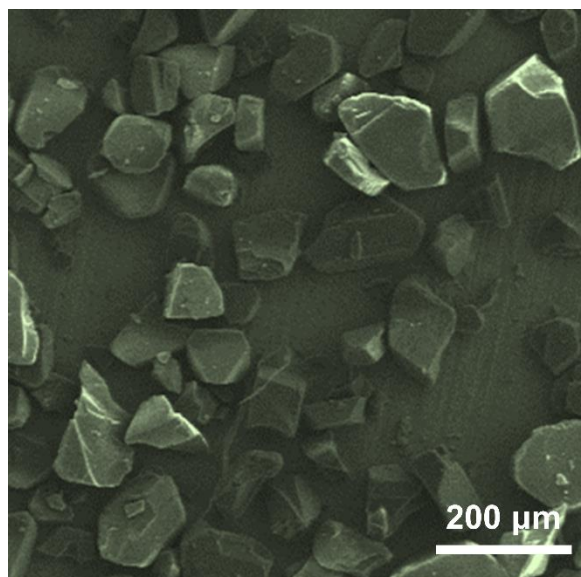


Figure S32. SEM image of micro powder of NTU-25.

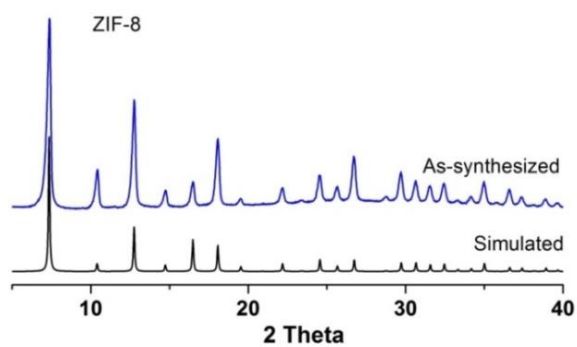


Figure S33. PXRD of ZIF-8: according to the refs of Chem. Commun , 2011, 47, 2071.

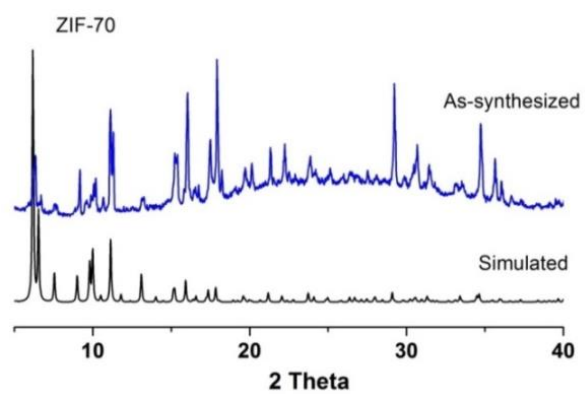


Figure S34. PXRD of ZIF-70: according to the refs of Science, 2008, 319, 939.

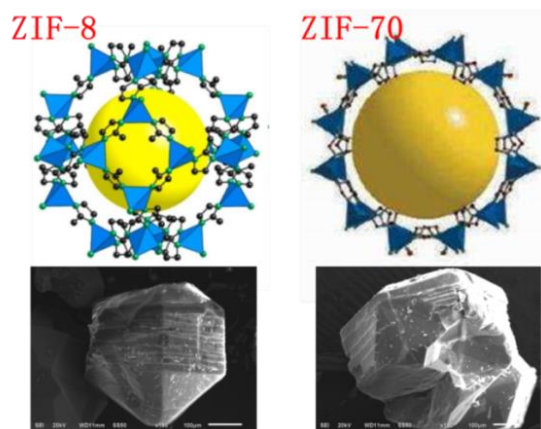


Figure S35. View of accessible pore of ZIF-8 ($1800 \text{ m}^2/\text{g}$) and ZIF-70 ($1730 \text{ m}^2/\text{g}$) that highlighted by yellow ball SEM image of their corresponded particles.

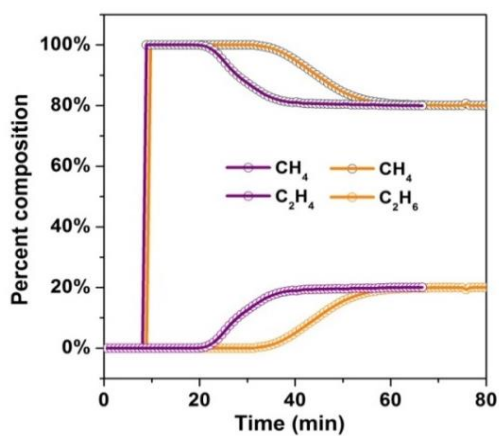


Figure S36. Breakthrough curves of $\text{C}_2\text{H}_4/\text{CH}_4$ and $\text{C}_2\text{H}_6/\text{CH}_4$ ($\text{V}/\text{V}= 20: 80$) in ZIF-8 at 273K. The breakthrough time was normalized to 1g from 605mg for easy comparison.

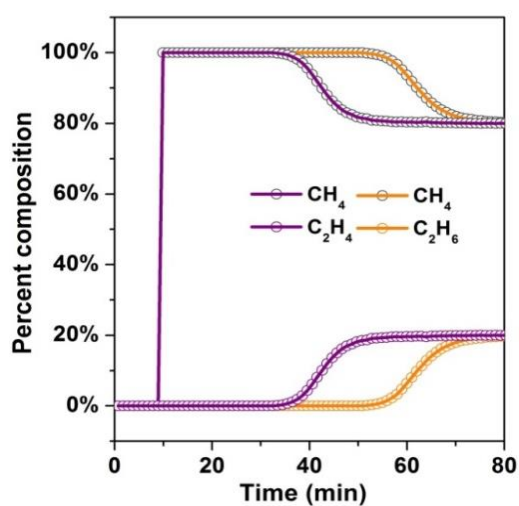


Figure S37. Breakthrough curves of ZIF-70 for $\text{C}_2\text{H}_4/\text{CH}_4$ and $\text{C}_2\text{H}_6/\text{CH}_4$ ($\text{V}/\text{V}= 20: 80$) at 273K. The breakthrough time was normalized to 1g from 487 mg for easy comparison.

Table S2. Breakthrough efficiency of C₂H₄/CH₄ on 1g of series of important PCPs.

	Mixtures	Gas speed(mL/min)	Break-through time (min)	16/22 4	Sample weight (g)	Breakthrough efficiency (mg/g)	Working condition	Refs
NTU-24	C ₂ H ₄ /CH ₄	8	67	0 7142	0 702	545 4	1 bar, 273K	This work
	C ₂ H ₆ /CH ₄	8	124	0 7142	0 702	1009 4	1 bar, 273K	
NTU-25	C ₂ H ₄ /CH ₄	8	88	0 7142	0 651	772 4	1 bar, 273K	
	C ₂ H ₆ /CH ₄	8	133 5	0 7142	0 651	1171 8	1 bar, 273K	
Broken NTU-25	C ₂ H ₄ /CH ₄	8	38 1	0 7142	0 525	414 7	1 bar, 273K	
	C ₂ H ₆ /CH ₄	8	66 5	0 7142	0 525	723 8	1 bar, 273K	
ZIF-8	C ₂ H ₄ /CH ₄	8	23 5	0 7142	0 603	222 7	1 bar, 273K	
	C ₂ H ₆ /CH ₄	8	41 9	0 7142	0 603	397 1	1 bar, 273K	
ZIF-70	C ₂ H ₄ /CH ₄	8	26 5	0 7142	0 487	310 9	1 bar, 273K	
	C ₂ H ₆ /CH ₄	8	44 1	0 7142	0 487	517 5	1 bar, 273K	
NTU-40	C ₂ H ₄ /CH ₄	8	9	0 7142	0 3	171 4	1 bar, 273K	3
	C ₂ H ₆ /CH ₄	8	12 1	0 7142	0 3	230 5	1 bar, 273K	
NTU-41	C ₂ H ₄ /CH ₄	8	4 2	0 7142	0 28	85 7	1 bar, 273K	
	C ₂ H ₆ /CH ₄	8	5 5	0 7142	0 28	112 2	1 bar, 273K	
CaX zeolite	C ₂ H ₄ /CH ₄	16	110	0 7142	16 33	77 0	1 bar, 298K	4
	C ₂ H ₆ /CH ₄	16	21	0 7142	16 33	14 7	1 bar, 298K	
LaBTB	C ₂ H ₆ /CH ₄	16	48 9	0 7142	4 578	976 6	8 bar, 273K	5
Mn(INA)	C ₂ H ₆ /CH ₄	16	6 5	0 7142	No data	No data	1 bar, 298K	
CID-5/6	C ₂ H ₆ /CH ₄	16	24	0 7142	No data	No data	8 bar, 273K	6
A-AC-3	C ₂ H ₆ /CH ₄	5	12	0 7142	0 2	196 3	1 bar, 298K	7
A-AC-4	C ₂ H ₆ /CH ₄	5	11 5	0 7142	0 2	188 1	1 bar, 298K	
Cu-TDPA	C ₂ H ₆ /CH ₄	8	2	0 7142	0 5	20 9	1 bar, 298K	8
ZnP-CTF-400	C ₂ H ₆ /CH ₄	No data	13	0 7142	No data	No data	30 bar, 298K	9
ZnP-CTF-500	C ₂ H ₆ /CH ₄	No data	15	0 7142	No data	No data	30 bar, 298K	
MAF-49	C ₂ H ₆ /CH ₄	No data	105	0 7142	No data	64 5	1bar, 313K	10

Note: The simulated breakthrough from single gas adsorption isotherms was not included here

References

- (1) Reed, A. E.; Weinstock, R. B.; Weinhold, F. Natural-Population Analysis. *J. Chem. Phys.* **1985**, *83*, 735-746.
- (2) Batsanov, S. S. Van der Waals radii of elements. *Inorg. Mater.* **2001**, *37*, 871-885.
- (3) Duan, J.; Zhang, Q.; Wang, S.; Zhou, B.; Sun, J.; Jin, W. Controlled flexibility of porous coordination polymers by shifting the position of the $-CH_3$ group around coordination sites and their highly efficient gas separation. *Inorg Chem Front* **2018**, *5*, 1780-1786.
- (4) Hosseinpour, S.; Fatemi, S.; Mortazavi, Y.; Gholamhoseini, M.; Ravanchi, M. T. Performance of CaX Zeolite for Separation of C_2H_6 , C_2H_4 , and CH_4 by Adsorption Process; Capacity, Selectivity, and Dynamic Adsorption Measurements. *Sep. Sci. Technol.* **2011**, *46*, 349-355.
- (5) Duan, J. G.; Higuchi, M.; Horike, S.; Foo, M. L.; Rao, K. P.; Inubushi, Y.; Fukushima, T.; Kitagawa, S. High CO_2/CH_4 and C-2 Hydrocarbons/ CH_4 Selectivity in a Chemically Robust Porous Coordination Polymer. *Adv. Funct. Mater.* **2013**, *23*, 3525-3530.
- (6) Horike, S.; Inubushi, Y.; Hori, T.; Fukushima, T.; Kitagawa, S. A solid solution approach to 2D coordination polymers for CH_4/CO_2 and CH_4/C_2H_6 gas separation: equilibrium and kinetic studies. *Chem. Sci.* **2012**, *3*, 116-120.
- (7) Liang, W.; Xiao, H.; Lv, D.; Xiao, J.; Li, Z. Novel asphalt-based carbon adsorbents with super-high adsorption capacity and excellent selectivity for separation for light hydrocarbons. *Sep. Purif. Technol.* **2018**, *190*, 60-67.
- (8) Liu, K.; Ma, D.; Li, B.; Li, Y.; Yao, K.; Zhang, Z.; Han, Y.; Shi, Z. High storage capacity and separation selectivity for C2 hydrocarbons over methane in the metal-organic framework Cu-TDPAT. *J. Mater. Chem. A* **2014**, *2*, 15823-15828.
- (9) Ma, H.; Ren, H.; Meng, S.; Sun, F.; Zhu, G. Novel porphyrinic porous organic frameworks for high performance separation of small hydrocarbons. *Sci. Rep.* **2013**, *3*, 2611-2617.
- (10) Liao, P. Q.; Zhang, W. X.; Zhang, J. P.; Chen, X. M. Efficient purification of ethene by an ethane-trapping metal-organic framework. *Nat. Commun.* **2015**, *6*, 8697-9705.